

# Stability Guarantees for Continuous RL Control

Bing Song<sup>1</sup>, Jean-Jacques Slotine<sup>2</sup> and Quang-Cuong Pham<sup>3</sup>

**Abstract**—Lack of stability guarantees strongly limits the use of reinforcement learning (RL) in safety critical robotic applications. Here we propose a control system architecture for continuous RL control and derive corresponding stability theorems via contraction analysis, yielding constraints on the network weights to ensure stability. The control architecture can be implemented in general RL algorithms and improve their stability, robustness, and sample efficiency. We demonstrate the importance and benefits of such guarantees for RL on two standard examples, PPO learning of a 2D problem and HIRO learning of maze tasks.

## I. INTRODUCTION

Reinforcement learning (RL) is expected to enable robots to learn multi-level reasoning tasks beyond the capability of classic control. However, lack of stability guarantee has prevented RL from stable performance comparable to classic control and hence wide applications in robotics, especially safety critical applications.

Here we propose a control architecture (Fig. 1) for continuous RL control and derive *stability theorems* for this architecture via contraction analysis [1]. Accordingly stability can be guaranteed by constraining the network weights. This architecture can be implemented in general RL algorithms to improve stability, robustness, and sample efficiency. For demonstration, we provide two examples: PPO [2] learning a 2D math problem and HIRO [3] learning maze tasks (Fig. 1).

A dynamic model  $\dot{y} = f(y, u, t)$  is required to compute the stability constraints. When this model only represents the robot dynamics, it can be obtained analytically or from learning. The implementation method for stability guarantee with a known model is in Section III.

When learning multi-level tasks, the model  $\dot{y} = f(y, u, t)$  represents not only the robot dynamics but also a high-level policy as well as other dynamics, if we want to use this architecture to guarantee stability for low-level control. In this case, the model is changing as learning progresses because of an updating high-level policy. It is infeasible to learn such a model by system identification simultaneously. Thus we propose to leverage impedance control techniques to make the end effector behave like a spring-mass-damper system in the Cartesian space. Based on this spring-mass-damper model made of controller gains, we can apply stability analysis. This can be used in low-level control for

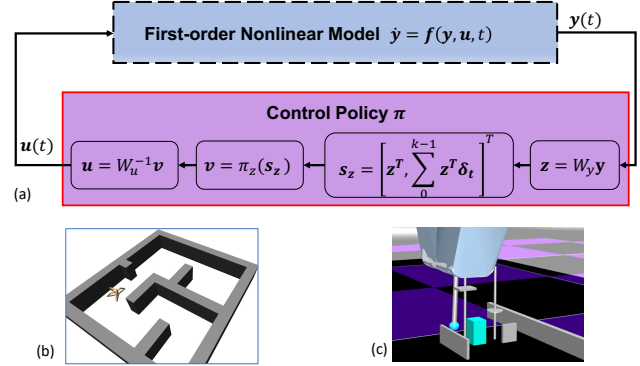


Fig. 1. Control system architecture for continuous RL control and multi-level tasks for demonstration. The control block diagram (a) is used to derive stability theorems via contraction analysis, which includes a coordinate transformation  $W_y$  and  $W_u$  as well as an inner policy  $\pi_z$ . We tested HIRO with stability guarantee via an ant maze (b) and a contact maze task (c).

hierarchical RL to learn multi-level tasks and improve its sample efficiency. The control block diagram of this method is plotted in Fig. 2 and the corresponding stability theorem is in Section IV.

To demonstrate our methods, we provide two examples: PPO learning a 2D math problem and HIRO learning maze tasks in Section V.

In the PPO example, we seek the answer to the question: does PPO learn some nonlinear controller as stable as classic control for this simple problem or a complex curve fitting from data which can not be extended for situations beyond training (e.g., longer running time for control)? Results show that PPO can learn stable control for this problem but very sensitive to neural network sizes and training time. Deteriorating performance is observed as training progresses after the initial convergence. With stability guarantee, PPO can maintain the stable performance regardless of training time as well as with a larger range of network sizes. PPO with stability guarantee also shows better robustness to model errors.

In the HIRO example, we want to examine if sample efficiency can be improved by constraining the low-level control inside the safe space. For the two maze tasks, HIRO with low-level stability guarantee outperforms the already-efficient original HIRO in sample efficiency. We also observed that the performance is very sensitive to the control architecture (Fig. 2) and we will perform an ablative study with respect to the architecture to analyze the learning dynamics.

Existing studies in stability usually use Lyapunov theory [4]. Here we use its differential counterpart: contraction the-

<sup>1</sup>Bing Song is with HP-NTU Digital Manufacturing Corporate Lab, Singapore, Singapore 639798, [bing.song@ntu.edu.sg](mailto:bing.song@ntu.edu.sg)

<sup>2</sup>Jean-Jacques Slotine is with Faculty of Mechanical Engineering, Massachusetts Institute of Technology, Cambridge MA 02139-4307, [jj@mit.edu](mailto:jj@mit.edu)

<sup>3</sup>Quang-Cuong Pham is with HP-NTU Digital Manufacturing Corporate Lab, Singapore, Singapore 639798, [cuong@ntu.edu.sg](mailto:cuong@ntu.edu.sg)

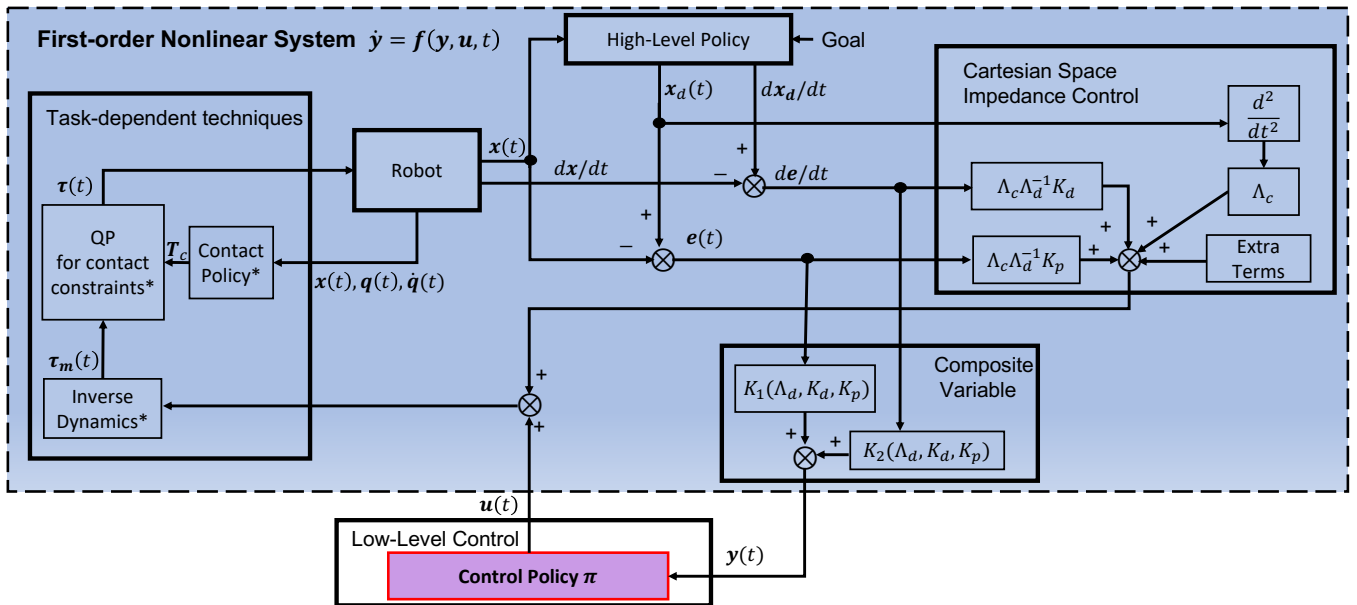


Fig. 2. Control block diagram for rigid body dynamics learning multi-level tasks. For multi-level tasks, the 1st-order nonlinear model represents not only the robot dynamics but also the high-level policy and so on. We leverage Cartesian space impedance control as well as other task-dependent control techniques to make the end effector behave like a spring-mass-damper system, i.e.,  $\Lambda_d \ddot{\mathbf{e}} + K_d \dot{\mathbf{e}} + K_p \mathbf{e} = -\mathbf{u}$ , where  $\mathbf{e} = \mathbf{x}_d - \mathbf{x}$  and  $\mathbf{u}$  is the low-level action. By defining a *composite variable*  $\mathbf{y}(t) = K_1 \mathbf{e}(t) + K_2 \dot{\mathbf{e}}(t)$ , we can obtain a 1st-order model  $\dot{\mathbf{y}} = \mathbf{f}(\mathbf{y}, \mathbf{u}, t)$  to compute the stability constraints.

ory [1]. The advantage of contraction analysis over Lyapunov is that it avoids to find a proper Lyapunov function and provides explicit sufficient conditions for stability in terms of generalized Jacobians.

Besides Lyapunov, some works have studied stability for specific systems or controllers [5], [6], which are less general than studies based on Lyapunov theory and contraction theory.

Contraction theory has been used in the research area of learning for system identification problems [7]–[9] or as a guidance [10]–[12] via Control Contraction Metrics (CCM) and its extensions [13]–[16], which are also applied in nonlinear control for stability [17], [18]. Unlike those works searching for stable solutions via CCM, we solve for the safe set of networks with respect to a given metric.

Instead of recursively searching in a safe set, we propose to limit the control network weights for stability, at the cost of complex in the control architecture (Fig. 1 and Fig. 2).

To our best knowledge, this is the first time that applies contraction analysis for continuous RL control.

## II. STABILITY THEOREM VIA CONTRACTION ANALYSIS

We derive the stability theorem based on the nonlinear model,

$$\begin{aligned} \dot{\mathbf{y}} &= \mathbf{f}(\mathbf{y}, \mathbf{u}, t) \\ \mathbf{u} &= \pi(\mathbf{y}) \end{aligned} \quad (1)$$

with respect to  $[\mathbf{y}^T \ \mathbf{u}^T]^T$ , where  $\mathbf{y} \in \mathcal{R}^m$  is the RL state;  $\mathbf{u} \in \mathcal{R}^m$  is the mean of the action distribution; and  $\pi$  denotes the control policy without stochastic sampling for exploration. We assume that with proper sampling strategies, the system remains stable with sampled actions if it is stable with  $\mathbf{u}$ .

Stability of nonlinear systems is generally defined relative to some nominal motion or equilibrium. Without requiring to know what the nominal motion is, contraction theory analyzes if a system is converging to the nominal motion regardless of initial conditions or temporary disturbances [1]. To simply put, if all trajectories converge to some unknown nominal motion in a region, this region is a contraction region; a system  $\dot{\mathbf{x}} = \mathbf{f}(\mathbf{x}, t)$  is contracting in a region, if its generalized Jacobian is uniformly negative in this region. The generalized Jacobian refers to the Jacobian with respect to some metric  $\mathbf{M}(\mathbf{x}, t)$  that is symmetric and continuously differentiable. Details are in Appendix VII-A.

With a control policy  $\pi$  of a particular architecture plotted in Figure 1, which includes

- a differential coordinate transformation

$$\mathbf{z} = W_y \mathbf{y}, \quad \mathbf{u} = W_u^{-1} \mathbf{v} \quad (2)$$

- an inner policy

$$\mathbf{v} = \pi_z(\mathbf{s}_z) \quad (3)$$

- the integral of  $\mathbf{z}$  as the input to the inner policy which is approximated by  $\sum_0^{k-1} \mathbf{z} \delta_t$ , where  $\delta_t$  is the sampling period for control

$$\mathbf{s}_z = \begin{bmatrix} \mathbf{s}_1 \\ \mathbf{s}_2 \end{bmatrix} = \begin{bmatrix} \mathbf{z} \\ \sum_0^{k-1} \mathbf{z} \delta_t \end{bmatrix} \quad (4)$$

we derive sufficient conditions for a system to be contracting in a region, i.e., stable in that region.

**Theorem 1.** Given a nonlinear system Eq. (1) and a control policy of the architecture in Fig. 1, if in a region

- $W_y$  and  $W_u$  are invertible that can form an uniformly positive definite metric  $\mathbf{M} = \Theta^T \Theta$  where

$$\Theta = \begin{bmatrix} W_y(\mathbf{y}, \mathbf{u}, t) & \\ & W_u(\mathbf{y}, \mathbf{u}, t) \end{bmatrix} \quad (5)$$

- there exists  $\epsilon > 0$  such that

$$(F_1^T + F_1) \prec -[\epsilon + \max(\nu^+, 0)]I \quad (6)$$

where  $\nu^+$  is the upper bound of eigenvalues of  $F_2^T + F_2$ ,

$$F_1 = \begin{bmatrix} W_y \frac{\partial \mathbf{f}}{\partial \mathbf{y}} W_y^{-1} & W_y \frac{\partial \mathbf{f}}{\partial \mathbf{u}} W_u^{-1} \\ \frac{\partial \pi_z}{\partial \mathbf{s}_1} W_y \frac{\partial \mathbf{f}}{\partial \mathbf{y}} W_y^{-1} + \frac{\partial \pi_z}{\partial \mathbf{s}_2} & \frac{\partial \pi_z}{\partial \mathbf{s}_1} W_y \frac{\partial \mathbf{f}}{\partial \mathbf{u}} W_u^{-1} \end{bmatrix} \quad (7)$$

$$F_2 = \begin{bmatrix} \dot{W}_y W_y^{-1} & 0 \\ \frac{\partial \pi_z}{\partial \mathbf{s}_1} \dot{W}_y W_y^{-1} & 0 \end{bmatrix}$$

this system Eq. (1) is contracting in that region.

*Proof.* The system dynamic Eq. (1) yields the differential relation

$$\delta \dot{\mathbf{y}} = \frac{\partial \mathbf{f}}{\partial \mathbf{y}}(\mathbf{y}, \mathbf{u}, t) \delta \mathbf{y} + \frac{\partial \mathbf{f}}{\partial \mathbf{u}}(\mathbf{y}, \mathbf{u}, t) \delta \mathbf{u} \quad (8)$$

where  $\delta \mathbf{y}$  and  $\delta \mathbf{u}$  are differential displacements, i.e., infinitesimal displacements at fixed time. The transformation Eq. (2) yields the differential relation

$$\begin{aligned} \delta \dot{\mathbf{z}} &= \dot{W}_y \delta \mathbf{y} + W_y \delta \dot{\mathbf{y}} \\ \delta \dot{\mathbf{u}} &= \dot{W}_u^{-1} \delta \mathbf{v} + W_u^{-1} \delta \dot{\mathbf{v}} \end{aligned} \quad (9)$$

The inner policy  $\pi_z$  Eq. (3) yields

$$\delta \dot{\mathbf{v}} = \frac{\partial \pi_z}{\partial \mathbf{s}_1} \delta \mathbf{s}_1 + \frac{\partial \pi_z}{\partial \mathbf{s}_2} \delta \mathbf{s}_2 \quad (10)$$

because  $\delta \dot{\mathbf{s}}_2 = \delta \mathbf{s}_1$ . Combining Eq. (8), Eq. (9), Eq. (10), and  $\mathbf{z} = \mathbf{s}_1$ , we obtain the equation in the Euclidean metric,

$$\begin{bmatrix} \delta \dot{\mathbf{y}} \\ \delta \dot{\mathbf{u}} \end{bmatrix} = J \begin{bmatrix} \delta \mathbf{y} \\ \delta \mathbf{u} \end{bmatrix} = \begin{bmatrix} \frac{\partial \mathbf{f}}{\partial \mathbf{y}} & \frac{\partial \mathbf{f}}{\partial \mathbf{u}} \\ J_{21} & J_{22} \end{bmatrix} \begin{bmatrix} \delta \mathbf{y} \\ \delta \mathbf{u} \end{bmatrix} \quad (11)$$

where

$$J_{21} = W_u^{-1} \frac{\partial \pi_z}{\partial \mathbf{s}_1} (\dot{W}_y + W_y \frac{\partial \mathbf{f}}{\partial \mathbf{y}}) + W_u^{-1} \frac{\partial \pi_z}{\partial \mathbf{s}_2} W_y \quad (12)$$

$$J_{22} = W_u^{-1} \frac{\partial \pi_z}{\partial \mathbf{s}_1} W_y \frac{\partial \mathbf{f}}{\partial \mathbf{u}} + \frac{d(W_u^{-1})}{dt} W_u$$

and the equation in the  $M = \Theta^T \Theta$  metric,

$$\begin{bmatrix} \delta \dot{\mathbf{z}} \\ \delta \dot{\mathbf{v}} \end{bmatrix} = F \begin{bmatrix} \delta \mathbf{z} \\ \delta \mathbf{v} \end{bmatrix} \quad (13)$$

where

$$F = \begin{bmatrix} [\dot{W}_y + W_y \frac{\partial \mathbf{f}}{\partial \mathbf{y}}] W_y^{-1} & W_y \frac{\partial \mathbf{f}}{\partial \mathbf{u}} W_u^{-1} \\ F_{21} & \frac{\partial \pi_z}{\partial \mathbf{s}_1} W_y \frac{\partial \mathbf{f}}{\partial \mathbf{u}} W_u^{-1} \end{bmatrix} \quad (14)$$

and

$$F_{21} = \frac{\partial \pi_z}{\partial \mathbf{s}_1} (\dot{W}_y + W_y \frac{\partial \mathbf{f}}{\partial \mathbf{y}}) W_y^{-1} + \frac{\partial \pi_z}{\partial \mathbf{s}_2} \quad (15)$$

This  $F = (\dot{\Theta} + \Theta J) \Theta^{-1}$  is the generalized Jacobian of Eq. (1) in the  $M$  metric. According to contraction theory [1]

(see Appendix VII-A), if  $F$  is uniformly negative definite in some region, the system Eq. (1) is contracting in the region.

We rewrite  $F$  into the sum of the constant  $F_1$  and the time-varying  $F_2$ . We denote the maximum eigenvalues of  $F_2^T + F_2$ ,  $F_1^T + F_1$ , and  $F^T + F$  by  $\nu^+$ ,  $\lambda^+$ , and  $\gamma^+$  respectively. Because  $\gamma^+ < \nu^+ + \lambda^+$ , given  $\epsilon > 0$ , if  $\lambda^+ < -(\epsilon + \nu^+)$ ,  $\gamma^+ < -\epsilon$ . Hence, a sufficient condition for uniformly negative definite  $F$  is that there exists  $\epsilon > 0$  such that  $\lambda^+ < -(\epsilon + \max(\nu^+, 0))$  in that region. Proof is finished.

According to *Theorem 1*, given a coordinate transformation and the system dynamic model, we can constrain the Jacobian of the inner policy ( $\partial \pi_z / \partial \mathbf{s}_1$  and  $\partial \pi_z / \partial \mathbf{s}_2$ ) for stability.

### III. STABILITY GUARANTEE FOR KNOWN SYSTEMS

According to *Theorem 1*, we need to solve Eq. (6) to find the constraints of  $\partial \pi_z / \partial \mathbf{s}_1$  and  $\partial \pi_z / \partial \mathbf{s}_2$  for stability. Here we specify  $W_y$ ,  $W_u$  and  $\pi_z$  to make the problem algebraically solvable. The first step is to transform Eq. (13) into the form, for example,

$$\begin{bmatrix} \delta \dot{z}_1 \\ \delta \dot{v}_1 \\ \delta \dot{z}_2 \\ \delta \dot{v}_2 \\ \delta \dot{z}_3 \\ \delta \dot{v}_3 \end{bmatrix} = \begin{bmatrix} A_1 & B_{12} & B_{13} \\ 0 & A_2 & B_{23} \\ 0 & 0 & A_3 \end{bmatrix} \begin{bmatrix} \delta z_1 \\ \delta v_1 \\ \delta z_2 \\ \delta v_2 \\ \delta z_3 \\ \delta v_3 \end{bmatrix} \quad (16)$$

For a system of the above form, if  $A_i$ 's are uniformly negative and  $B_{ij}$ 's are bounded, the system Eq. (1) is contracting [1]. By solving the characteristic functions of  $A_i$ 's, we obtain the boundaries of network weights for stability. This is *Theorem 2* and its proof is in Appendix VII-B.

**Theorem 2.** With the following designs,

- $W_y$ : the normalized eigenvector matrix of  $\partial \mathbf{f} / \partial \mathbf{y}$
- $W_u$ :  $W_u = PQ^T$  where  $Q$  is from the QR decomposition of  $P(W_y \partial \mathbf{f} / \partial \mathbf{u})$  and  $P$  is a permutation matrix with all ones at the skew diagonal
- $\pi_z$ : a parallel sequence of independent neural networks denoted by  $h_i$  as in Figure. 3

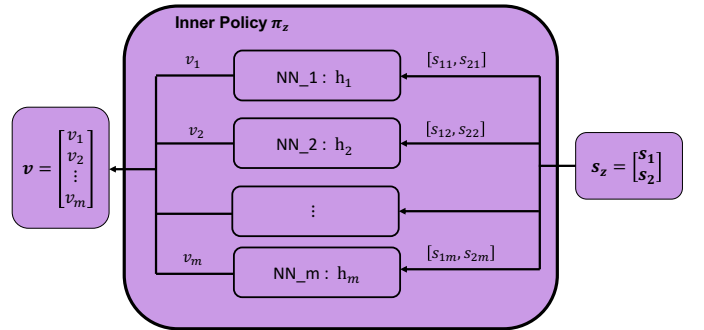


Fig. 3. The inner policy  $\pi_z$  inside the control policy  $\pi$  (Fig. 1) is made of a parallel sequence of independent neural networks  $h_i$ , the inputs of which are  $[s_{1i} \ s_{2i}] = [z_i \ \sum_{t=0}^{k-1} z_i \delta t]$  where  $i = 1, 2, \dots, m$ .

and the assumption that  $\dot{W}_y$  can be ignored and the partial derivatives of  $\pi_z$  are bounded, for a system Eq. (1) with

diagonalizable  $\partial \mathbf{f} / \partial \mathbf{y}$ , if in a region there exists  $\epsilon > 0$  that

$$\frac{\partial h_i}{\partial s_{1i}} b_{ii} + \lambda_i < -\epsilon, \quad \frac{\partial h_i}{\partial s_{2i}} b_{ii} < -\epsilon \quad (17)$$

where  $\lambda_i$  is the  $i$ th eigenvalue of  $\partial \mathbf{f} / \partial \mathbf{y}$ ,  $b_{ii}$  is the  $i$ th diagonal component of  $W_y (\partial \mathbf{f} / \partial \mathbf{u}) W_u^{-1}$ , the system Eq. (1) is contracting in that region.

Given the bounds of  $\lambda_i$  and  $b_{ii}$ , *Theorem 2* provides inequality constraints with respect to  $\partial h_i / \partial s_{ij}$  ( $i = 1, 2$  and  $j = 1, 2, \dots, m$ ).

Here we propose an implementation method of *Theorem 2* (the learning algorithm remains the same):

- Apply control techniques to make the system stable when the RL actions are equal to zero, i.e.  $\dot{\mathbf{y}} = \mathbf{f}(\mathbf{y}, 0, t)$  converging to some equilibrium as time progresses. This means  $\lambda_i \leq 0$  otherwise the solution to the differential equation  $\delta \dot{\mathbf{y}} = \partial \mathbf{f} / \partial \mathbf{y} \delta \mathbf{y}$  contains a diverging component  $e^{\lambda_i t}$  which is contradict to the premise that the system is converging. This is generally true for robotic systems in real world.
- Use a control policy of the architecture in Fig. 1 and use the inner policy of the architecture in Fig. 3 with multilayer perceptron networks (MLPs) (e.g., with tanh as activation functions) as  $h_i$ 's ( $i = 1, 2, \dots, m$ ). In this case,  $\partial h_i / \partial s_{ij}$  ( $i = 1, 2$  and  $j = 1, 2, \dots, m$ ) becomes the product of the network weights scaled by the derivative of the activation function.
- Set the weights of an  $l$ -layered network  $h_i$  as follows. For the  $j$ th layer ( $j = 1, 2, \dots, l - 1$ ), the weights are bigger than some small positive number  $\epsilon$ . For the last layer, the weights are bigger than  $-\epsilon b_{ii} / \|b_{ii}\|$  if  $b_{ii} < 0$  or smaller than  $-\epsilon b_{ii} / \|b_{ii}\|$  if  $b_{ii} > 0$ . In code, this can be implemented by constraining the weights by  $\epsilon$  and adding another operation that multiplies the opposite sign of  $b_{ii}$ .

With this implementation and the assumptions in *Theorem 2*, the system is contracting except at the points with a saturating activation function. Proof is in Appendix VII-C. With a saturating activation function, the RL action becomes a constant  $\mathbf{u}_{const}$  and  $\dot{\mathbf{y}} = \mathbf{f}(\mathbf{y}, \mathbf{u}_{const}, t)$ , which requires pre-designed control techniques and a proper range of RL actions for stability.

When there exists model errors in  $b_{ii}$  and  $\lambda_i$ , as long as the inequalities Eq. (17) hold, the system remains stable.

#### IV. STABILITY GUARANTEE FOR UNKNOWN SYSTEMS: RIGID BODY DYNAMICS LEARNING MULTI-LEVEL TASKS

For rigid body dynamics to learn multi-level tasks via hierarchical RL, it is infeasible to learn the nonlinear model that includes the high level policy. Thus we leverage Cartesian-space impedance control to make the end-effectors behave like a spring-mass-damper system,

$$\Lambda_d \ddot{\mathbf{e}} + K_d \dot{\mathbf{e}} + K_p \mathbf{e} + K_{rl} \mathbf{u}_{rl} = 0 \quad (18)$$

where  $\mathbf{e} = \mathbf{x}_d - \mathbf{x}$  denotes the tracking error of the end effectors,  $\mathbf{x}_d$  is the high-level RL action,  $\Lambda_d$ ,  $K_d$ , and  $K_p$  are the controller gains,  $K_{rl}$  is the weights for the feed-forward

low-level RL actions. We used techniques from [19]–[21] to build the control diagram in Fig. 2 (see Appendix VII-D).

We then use a *composite variable*,

$$\mathbf{y} = K_1 \mathbf{e} + K_2 \dot{\mathbf{e}} \quad (19)$$

to decrease the order of Eq. (18). Plugging Eq. (19) into Eq. (18), the dynamic model becomes

$$\Lambda_y \dot{\mathbf{y}} + B_y \mathbf{y} + K_{rl} \mathbf{u}_{rl} = 0 \quad (20)$$

where  $K_1$ ,  $K_2$ ,  $\Lambda_y$  and  $B_y$  are positive definite diagonal matrices made of  $\Lambda_d$ ,  $K_d$ , and  $K_p$ :

- when  $K_p = 0$ , we use  $K_2 = K_d$  and  $K_1 = 0$  which results in

$$\Lambda_y = \Lambda_d, \quad B_y = K_d \quad (21)$$

- otherwise we use

$$K_{1,i} = \frac{K_{p,i}}{\lambda_{d,i}}, \quad K_{2,i} = \frac{2K_{p,i}}{K_{d,i} \pm \sqrt{K_{d,i}^2 - 4K_{p,i}\lambda_{d,i}}} \quad (22)$$

where the subscript  $i$  denotes the  $i$ th diagonal element of the matrix, requiring  $K_{d,i}^2 - 4K_{p,i}\lambda_{d,i} \geq 0$ . Note that we have positive definite  $K_1$  and  $K_2$  given stable controllers with positive definite  $\Lambda_d$ ,  $K_d$  and  $K_p$ . The resulting coefficient matrices in Eq. (20) becomes

$$\Lambda_y = \Lambda_d K_2^{-1}, \quad B_y = \Lambda_d \quad (23)$$

are positive definite diagonal matrices since  $\Lambda_d$ ,  $K_2$  are positive definite diagonal matrices.

This linear model Eq. 20 can be used as the system model in *Theorem 2*.

However, this model Eq. 20 suffers from nonlinear errors (denoted by  $\zeta$ ),

$$\Lambda_y \dot{\mathbf{y}} + B_y \mathbf{y} + K_{rl} \mathbf{u}_{rl} = \zeta(\mathbf{q}, \dot{\mathbf{q}}, \ddot{\mathbf{q}}) \quad (24)$$

Hence we propose to use *absorbing matrices* to evaluate the robustness. If there exists time-varying diagonal matrices  $\tilde{\Lambda}_y \succ 0$  and  $\tilde{B}_y \succ 0$  that satisfies

$$\zeta(\mathbf{q}, \dot{\mathbf{q}}, \ddot{\mathbf{q}}) + (\tilde{\Lambda}_y - \Lambda_y) \dot{\mathbf{y}} + (\tilde{B}_y - B_y) \mathbf{y} = 0 \quad (25)$$

where positive definite matrices  $\Lambda_y$  and  $B_y$  are in Eq. 23 in Appendix VII-E, the system remains stable.

We summarize the above discussions into *Theorem 3* and its proof is in Appendix VII-E. The implementation is to first apply the control architecture in Fig. 2 and then follow the implementation method of *Theorem 2*.

**Theorem 3** For rigid body dynamics to learn multi-level tasks via hierarchical RL, with the control diagram in Fig. 2 implemented for low-level control, with the assumption that the partial derivatives of  $\pi_z$  are bounded, if in a region

- there exists  $\tilde{\Lambda}_y \succ 0$  and  $\tilde{B}_y \succ 0$  that satisfies Eq. (25)
- there exists  $\epsilon > 0$  that

$$\frac{\partial h_i}{\partial z_i} K_{rl,i} > \epsilon, \quad \frac{\partial h_i}{\partial (\sum_0^{k-1} z_i)} K_{rl,i} > \epsilon \quad (26)$$

where  $K_{rl,i}$  is the  $i$ th diagonal component of  $K_{rl}$

the system with respect to the composite variable Eq. (24) is contracting.

By solving Eq. (19) with positive definite  $K_1$  and  $K_2$ , the tracking error is converging to zero with some transients when the composite variable is converging to zero, that is, asymptotically stable.

## V. EXPERIMENTS

We demonstrate our methods on two algorithms: (a) PPO learning a 2D math example and (b) HIRO for rigid body dynamics learning maze tasks. We tested 5 different seeds for training. Environment and implementation details are in Appendix VII-F.

### A. PPO vs PPO with stability guarantee (C-PPO)

In the 2D math example with known  $\partial f/\partial \mathbf{y}$  and  $\partial \mathbf{y}/\partial \mathbf{u}$ , we apply *Theorem 2* for stability guarantee.

The 2D math example approximates a peg with 1st-order dynamics moving in a perpendicular plane to touch  $x_d$  with force  $f_d$  ( $x_d$  and  $f_d$  are randomly sampled),

$$\begin{aligned} \tau_z \dot{z} + z &= u_z \\ \tau_x \dot{x} + x &= u_x \\ f &= K_{sur} \min(z - g(x), 0) \end{aligned} \quad (27)$$

where the surface profile  $g(x) = K_1 \sin(x) + K_2 \cos(x)$ . The reward is a weighted sum of penalties on negative distance and chattering motions.

To answer the question, does PPO learn some nonlinear controller as stable as classic control or a complex curve fitting from data which can not be extended for situations beyond training? We design the experiments as follows:

- PPO is considered to have learned some stable nonlinear controller (i.e., a stable learned policy) if the tracking accuracy can be kept for extended controller running time in the tests. The control policy was running 8 s in training (8 second trajectories) but tested for 16 s. The target was sampled in a range that can be reached within a short time much less than 8 s. We checked the resulting trajectories and most of them have reached the goals in 2 s. This implies that 8 s is reasonably long enough to learn this math problem.
- Different neural network sizes, different definitions of RL states, and other parameters are tested to find the best performance of PPO without stability guarantee. The best performance is on the same level as PPO with stability guarantee (named C-PPO). The settings with the best performance are used for the stability and robustness test.

*Stability test.* After the initial convergence of PPO and C-PPO (learning curves of episodes vs negative expected returns are plotted in Fig. 4 (c)), we tested the learned policy every 1k episodes, from Episode 4000 until 9000. An increasing percentage of failed trajectories (error larger than 0.4) is observed for PPO (Fig. 4 (a)) as training progresses. We observed three types of failed trajectories:

- Chattering motions Fig. 4 (b) and (d). Chattering motions are related to  $\partial f/\partial \mathbf{u}$  of Eq. (1), the value of which changes on a large scale for the task.
- Non-zero equilibrium Fig. 4 (f). To avoid non-zero equilibrium, we propose *Theorem 4* in Appendix VII-F.1.c.
- Drifting away Fig. 4 (e). Some trajectories drift away after 8 s, which implies that the networks have learned to cancel the errors for each data point of a trajectory but failed to learn a stable controller.

On the other hand, C-PPO maintains the tracking accuracy in the stability test. With stability guarantee, we limit the network to approximate a stable state-dependent PI controller instead of unlimited nonlinear curve fittings to cancel the errors.

*Robustness test.* We tested robustness of the learned policy at Episode 4000 for PPO and Episode 5500 for C-PPO, with 50% error in  $\tau_i$  ( $i = x, z$ ), 100% in  $K_{sur}$  and 50% in  $K_i$  ( $i = 1, 2$ ). The histograms of tracking errors are plotted in Fig. 5. C-PPO shows much better robustness to model errors.

For this simple problem, PPO without stability guarantee can learn a stable control policy with a network size  $3 \times 32$  after initial convergence at Episode 4000. But the performance deteriorates as training progresses. With stability guarantee, C-PPO maintains the stable performance. C-PPO also shows improved robustness to model errors compared to a stable PPO policy. We also observed that C-PPO can learn with a much larger network size (Fig. 6).

### B. HIRO vs HIRO with low-level stability guarantee (C-HIRO)

We implemented the control architecture in Fig. 2 for HIRO and applied *Theorem 3* to learn two tasks: an ant maze and a contact maze (Fig. 1). Since HIRO can learn the original ant-maze benchmark task well, we increased the difficulty of the ant-maze task by making a less structured maze, starting with random initial positions in the maze to reach randomly sampled goals, and adding one more joint for each leg. In the contact maze task, the end-effector is supposed to reach a randomly sampled goal in the green box without vision (Fig. 1 (c)). Details of our implementation are in Appendix VII-D.2, VII-D.3, and VII-F.

In both example, C-HIRO shows better sample efficiency (Fig. 7). The reasons of the improvement are three-pronged: (a) stability constraints decrease the exploration space for low-level control; (b) the high-level action is in the Cartesian space instead of the high-dimensional generalized coordinates; and (c) low-level actions with stability guarantee may alleviate the non-stationary issue for the high-level policy.

We also observed that the performance is very sensitive to the control architecture in Fig. 2. For example, with different desired speeds, C-HIRO reached around 30% to 70% success of the ant maze problem in 10M steps, although both higher than HIRO. This may be related to violations of assumptions in the theorems or the interaction between learning dynamics and the control system dynamics. We will perform ablative

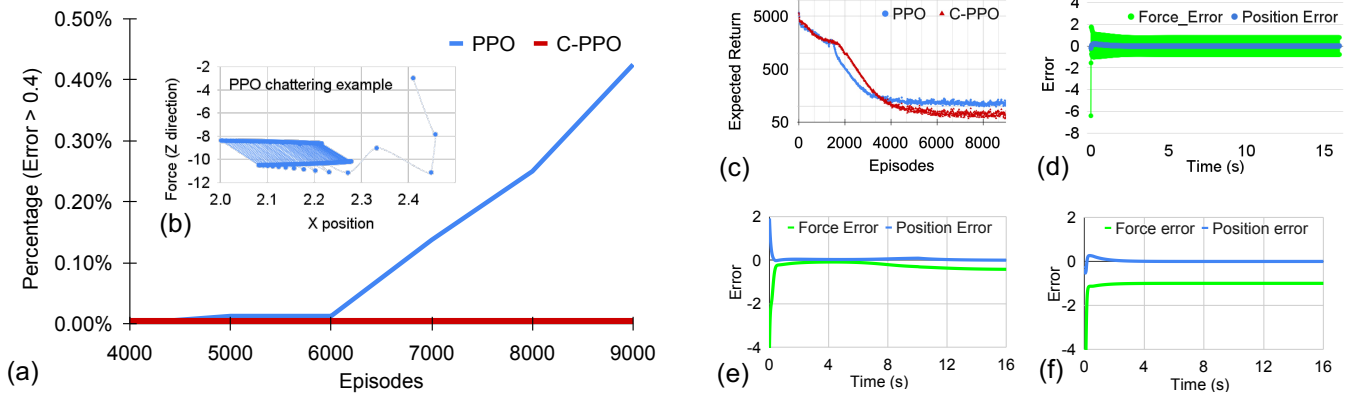


Fig. 4. Stability of PPO vs PPO with stability guarantee (C-PPO). In the stability test, we extended the controller running time (trajectory length) from 8 s to 16 s to examine if PPO can perform classic-control level stability or if PPO learns a complex curve fitting from data. We used the setting with which PPO has achieved the best performance in our hyper-parameters search. With this setting, PPO has achieved the same level of tracking accuracy as C-PPO after initial convergence. With the stable learning curves in (c) that show both PPO and C-PPO have learned the task reasonably well, a seemingly well-learned PPO policy without stability guarantee has deteriorating performance, i.e., an increasing percentage of failed trajectories in testing as training progresses, plotted in (a). Three types of failures are observed: (b) and (d) plot the chattering motions; (e) plots a trajectory drifting away; (f) plots a trajectory staying at a non-zero equilibrium. On the other hand, C-PPO maintains stable performance.

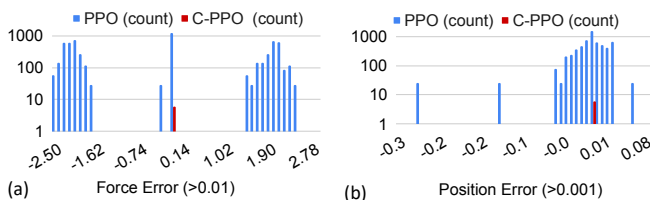


Fig. 5. Robustness of PPO vs PPO with stability guarantee (C-PPO). With 50% model errors in  $\tau_i$  ( $i = x, z$ ), 100% in  $K_{sur}$  and 50% in  $K_i$  ( $i = 1, 2$ ), the histograms of errors from 8000 randomly sampled trials of stable policies are plotted in (a) and (b). The largest errors from C-PPO are under 0.1 (force) and 0.01 (position), while PPO shows less robustness: the largest are around 2.5 and 0.25.

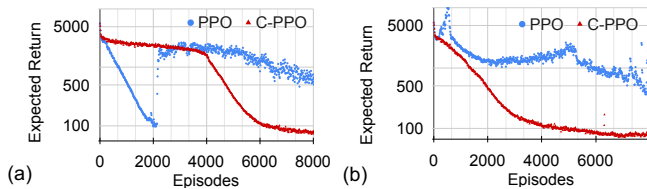


Fig. 6. Learning with different NN sizes: PPO vs PPO with stability guarantee (C-PPO). With gradually increasing network sizes (the value and control networks) from  $3 \times 32$  until  $3 \times 512$ , PPO fails to learn at  $3 \times 256$  (learning curves in (a)), while C-PPO shows some instabilities in learning at  $3 \times 512$  and when we changed the value network to  $3 \times 32$  and kept the control networks to be  $3 \times 512$ , C-PPO learns steadily again (learning curves in (b)).

study, analyze the learning dynamics, and further leverage control and path planning to learn multi-level tasks.

## VI. CONCLUDING REMARKS

By employing the control architecture in Fig. 1, contraction theory can be applied for stability analysis of continuous RL control, yielding stability constraints on network weights. The stability analysis requires a first-order nonlinear model

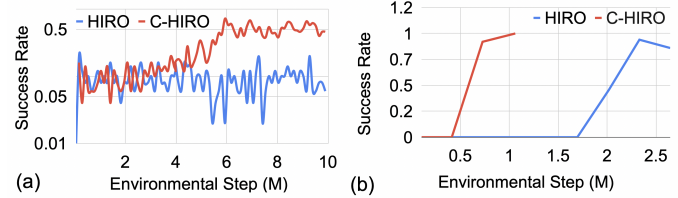


Fig. 7. Success rates of HIRO vs HIRO with low-level stability guarantee (C-HIRO). The success rate is computed from 50 random trials. In the ant maze test, C-HIRO reached a  $\sim 60\%$  success rate in 10M steps while HIRO reached  $\sim 10\%$ . For the following 5M steps, both stayed on those levels. In the contact maze test, C-HIRO found the paths in 1M steps while HIRO took 2.5M steps.

$\dot{y} = f(y, u, t)$  that describes the mapping from  $u$  to  $y$ , which may include different physical dynamics and algorithms. Leveraging existing control techniques can create such a model with respect to the end effector behaviors in the Cartesian space. This paper demonstrates the importance and benefits of such stability guarantees for RL. Current research focuses on the control system dynamics. In future, we will expand our study to the learning dynamics, i.e., optimization of control policies.

## VII. APPENDIX

### A. Contraction theory

Here we present the theorem from contraction theory [1] that is used in this paper.

a) *Definition of a contraction region:* Given the system equations  $\dot{x} = f(x, t)$ , a region of the state space is called a contraction region with respect to a uniformly positive definite metric  $M(x, t) = \Theta^T \Theta$ , if equivalently the generalized Jacobian  $F = (\Theta + \Theta \partial f / \partial x) \Theta^{-1}$  is uniformly negative definite in that region.

b) *Theorem:* Given the system equations  $\dot{x} = f(x, t)$ , any trajectory, which starts in a ball of constant radius with

respect to the metric  $\mathbf{M}(\mathbf{x}, t)$ , centered at a given trajectory and contained at all times in a contraction region with respect to  $\mathbf{M}(\mathbf{x}, t)$ , remains in that ball and converges exponentially to this trajectory. Furthermore global exponential convergence to the given trajectory is guaranteed if the whole state space is a contraction region with respect to the metric  $\mathbf{M}(\mathbf{x}, t)$ .

### B. Proof of Theorem 2

For a system of the form

$$\frac{d}{dt} \begin{bmatrix} \mathbf{z}_1 \\ \mathbf{z}_2 \end{bmatrix} = \begin{bmatrix} F_{11} & F_{12} \\ 0 & F_{22} \end{bmatrix} \begin{bmatrix} \mathbf{z}_1 \\ \mathbf{z}_2 \end{bmatrix} \quad (28)$$

assuming that  $F_{12}$  is bounded, with uniformly negative definite  $F_{11}$  and  $F_{22}$ , the whole system globally exponentially converges to some nominal trajectory, which can be extended to systems similarly partitioned in more than two equations [1].

Firstly, we prove that with the proposed  $W_y$ ,  $W_u$ , and  $\pi_z$ , Eq. (13) can be reorganized into the form of a hierarchical combination Eq. (16). For a system Eq. (1) with diagonalizable  $\partial \mathbf{f} / \partial \mathbf{y}$ , when  $W_y$  is the normalized eigenvector matrix,  $W_y(\partial \mathbf{f} / \partial \mathbf{y})W_y^{-1}$  becomes the diagonal eigenvalue matrix, denoted by  $\Lambda$ . With the proposed  $W_u$ , we can obtain an upper triangular  $W_y(\partial \mathbf{f} / \partial \mathbf{u})W_u^{-1}$  (denoted by  $B$ ). Here we not only show the QR decomposition method in the paper, but also provide another method: LU decomposition.

- QR decomposition. One can use

$$\begin{aligned} X &= P(W_y \frac{\partial \mathbf{f}}{\partial \mathbf{u}}) \\ X^T &= QR \\ W_u &= PQ^T \end{aligned} \quad (29)$$

where  $P$  is a permutation matrix

$$P = \begin{bmatrix} & & & 1 \\ & & \cdot & \\ & & & \\ 1 & & & \end{bmatrix} \quad (30)$$

The resulting  $B$  becomes

$$\begin{aligned} B &= W_y \frac{\partial \mathbf{f}}{\partial \mathbf{u}} W_u^{-1} \\ &= P(PW_y \frac{\partial \mathbf{f}}{\partial \mathbf{u}} (PQ^T)^{-1}) \\ &= P(QR)^T (Q^T)^{-1} P \\ &= PR^T P \end{aligned} \quad (31)$$

which is an upper diagonal matrix.

- LU decomposition. One can use

$$\begin{aligned} P(\tilde{W}_e \frac{\partial \mathbf{f}}{\partial \mathbf{u}})P &= LU \\ W_u &= PUP^T \end{aligned} \quad (32)$$

The resulting  $B = PLP$ .

With a diagonal  $\Lambda = W_y(\partial \mathbf{f} / \partial \mathbf{y})W_y^{-1}$  and an upper triangular  $B = W_y(\partial \mathbf{f} / \partial \mathbf{u})W_u^{-1}$ , if  $\dot{W}_y$  can be ignored, the

resulting system can be written into a hierarchical combination as follows. With the assumption that  $\dot{W}_y$  can be ignored, Eq. (13) becomes

$$\begin{bmatrix} \delta \dot{\mathbf{z}} \\ \delta \dot{\mathbf{v}} \end{bmatrix} = \begin{bmatrix} \Lambda & B \\ \frac{\partial \pi_z}{\partial \mathbf{s}_1} \Lambda + \frac{\partial \pi_z}{\partial \mathbf{s}_2} & \frac{\partial \pi_z}{\partial \mathbf{s}_1} B \end{bmatrix} \begin{bmatrix} \delta \mathbf{z} \\ \delta \mathbf{v} \end{bmatrix} \quad (33)$$

Eq. (33) (an example with two real eigenvalues of  $\partial \mathbf{f} / \partial \mathbf{y}$ ) can be reorganized into a hierarchical combination of equations with respect to  $[\delta z_i \quad \delta v_i]$

$$\begin{bmatrix} \delta \dot{z}_1 & \delta \dot{v}_1 & | & \delta \dot{z}_2 & \delta \dot{v}_2 \end{bmatrix}^T = \left[ \begin{array}{cc|cc} \lambda_1 & b_{11} & 0 & b_{12} \\ \frac{\partial h_1}{\partial s_{11}} \lambda_1 + \frac{\partial h_1}{\partial s_{21}} & \frac{\partial h_1}{\partial s_{11}} b_{11} & 0 & \frac{\partial h_1}{\partial s_{11}} b_{12} \\ \hline 0 & 0 & \lambda_2 & b_{22} \\ 0 & 0 & \frac{\partial h_2}{\partial s_{12}} \lambda_2 + \frac{\partial h_2}{\partial s_{22}} & \frac{\partial h_2}{\partial s_{12}} b_{22} \end{array} \right] \begin{bmatrix} \delta z_1 \\ \delta v_1 \\ \delta z_2 \\ \delta v_2 \end{bmatrix} \quad (34)$$

According to contraction theory for hierarchical combination, if the diagonal blocks are uniformly negative definite in a region and the off-diagonal blocks are bounded, the system is contracting in the region. By solving their characteristic equation

$$s^2 - (\lambda_i + \frac{\partial h_i}{\partial s_{1i}} b_{ii})s + b_{ii} \frac{\partial h_i}{\partial s_{2i}} = 0 \quad (35)$$

we obtain that if there exists  $\epsilon > 0$ ,

$$\frac{\partial h_i}{\partial s_{1i}} b_{ii} + \lambda_i < -\epsilon, \quad \frac{\partial h_i}{\partial s_{2i}} b_{ii} < -\epsilon \quad (36)$$

the diagonal blocks are uniformly negative definite. The off-diagonal blocks are bounded, with bounded  $\partial f / \partial \mathbf{u}$ , invertible  $W_y$  and  $W_u$ , and bounded  $\partial h_i / \partial s_{1i}$ . Proof is finished.

One can extend this for systems with complex eigenvalues. In that case, to algebraically compute the range of the safe set is non trivial. Moreover, one might extend the theorems for repeated eigenvalues by using Jordan canonical form in future, which currently in implementation is numerically unstable.

### C. Proof of the stability guarantee with the implementation method in Section III

Given  $\lambda_i \leq 0$ , the inequality Eq. (17) in Theorem 2 can be further simplified into

$$\frac{\partial h_i}{\partial s_{1i}} b_{ii} < -\epsilon, \quad \frac{\partial h_i}{\partial s_{2i}} b_{ii} < -\epsilon \quad (37)$$

because

$$\frac{\partial h_i}{\partial s_{1i}} b_{ii} < -\epsilon \leq -\epsilon - \lambda_i \quad (38)$$

Thus if Eq. (37) is satisfied, the inequalities in Theorem 2 are satisfied.

For each pair of equations of  $z$ , we use an independent MLP with the hyperbolic tangent function as the activation

function for control. The resulting  $\pi_z$  then becomes

$$\mathbf{v} = \begin{bmatrix} v_1 \\ v_2 \\ \vdots \\ v_m \end{bmatrix} = \pi_z(\mathbf{s}_{\mathbf{s}_1}) = \begin{bmatrix} h_1([s_{11}, s_{21}]) \\ h_2([s_{12}, s_{22}]) \\ \vdots \\ h_m([s_{1m}, s_{2m}]) \end{bmatrix} \quad (39)$$

where  $h_i$  denotes a MLP. The partial derivatives  $\partial\pi_z/\partial\mathbf{s}_1$  and  $\partial\pi_z/\partial\mathbf{s}_2$  become diagonal matrices, the diagonal components of which are the products of weights and  $[1 - \tanh^2(\cdot)]$ 's.

For the  $j^{\text{th}}$  layer of the  $i^{\text{th}}$  MLP,  $x_{j+1} = \tanh(W_j x_j + b_j)$  where  $W_j$  denotes the weights. For the first layer, we also denote the weights corresponding to  $s_{i1}$  and  $s_{i2}$  respectively by  $W_{1,1}$  and  $W_{1,2}$ . The partial derivative with respect to  $s_{i1}$  becomes

$$\frac{\partial h_i}{\partial s_{i1}} = W_l M_{l-1} W_{l-1} \cdots M_2 W_2 M_1 W_{1,1} \quad (40)$$

where  $M_j = 1 - \tanh^2(W_j x_j + b_j)$ . When the activation function is not saturated, we denote the lower bound of the components of  $M_j$ 's by  $\epsilon_m$ .

With the proposed weight constraints (the lower bounds are all small positive values), the components of the product in Eq. 40 without the last layer, i.e.,  $(M_{l-1} W_{l-1} \cdots M_2 W_2 M_1 W_{1,1})$  is bigger than some positive value  $\epsilon_1$ . With  $k$  nodes in the last layer,

$$\begin{aligned} & \frac{\partial h_i}{\partial s_{i1}} b_{ii} \\ &= W_l (M_{l-1} W_{l-1} \cdots M_2 W_2 M_1 W_{1,1}) b_{ii} \\ &< -k\epsilon_1 \epsilon \frac{b_{ii}^2}{\|b_{ii}\|} \end{aligned} \quad (41)$$

when

$$\begin{cases} W_{li} > -\epsilon b_{ii} / \|b_{ii}\| & \text{when } b_{ii} < 0 \\ W_{li} < -\epsilon b_{ii} / \|b_{ii}\| & \text{when } b_{ii} > 0 \end{cases} \quad (42)$$

$$(M_{l-1} W_{l-1} \cdots M_2 W_2 M_1 W_{1,1})_i > \epsilon_1$$

where the subscript  $i$  denotes the  $i^{\text{th}}$  component of the vector. Note that  $b_{ii} = 0$  means the system dynamics cannot be controlled by the RL policy, which is not considered in our discussion.

So there exists a small positive number  $k\epsilon_1 \epsilon b_{ii}^2 / \|b_{ii}\|$  that the inequality in terms of  $s_{1i}$  in Eq. 37 is satisfied. This proof can be also used for  $s_{2i}$ .

#### D. Control architecture in Fig. 2

1) *Rigid body dynamics*: We consider two types of rigid body dynamics: with a fixed or a floating base.

- Fixed base:

$$H(\mathbf{q})\ddot{\mathbf{q}} + C(\mathbf{q}, \dot{\mathbf{q}})\dot{\mathbf{q}} + \mathbf{g}(\mathbf{q}) = \boldsymbol{\tau} + J^T(\mathbf{q})\boldsymbol{\gamma} \quad (43)$$

where  $\mathbf{q} \in \mathbb{R}^n$  is the vector of joint angles,  $\boldsymbol{\tau}$  represents the torques applied on joints,  $\boldsymbol{\gamma}$  represents the wrench at the end effector,  $H$  is the mass matrix,  $C(\mathbf{q}, \nu)$  and  $g(\mathbf{q})$  are the Coriolis, centrifugal, and gravitational terms.

- Floating base:

$$H(\mathbf{q})\dot{\boldsymbol{\nu}} + C(\mathbf{q}, \boldsymbol{\nu}) + \mathbf{g}(\mathbf{q}) = S^T \boldsymbol{\tau}_c + J_c^T(\mathbf{q})\boldsymbol{\gamma}_c \quad (44)$$

where

$$\mathbf{q} = \begin{pmatrix} \boldsymbol{\xi}_b \\ \boldsymbol{\theta} \end{pmatrix}, \boldsymbol{\nu} = \begin{bmatrix} \mathbf{v}_b \\ \dot{\boldsymbol{\theta}} \end{bmatrix}, S = \begin{bmatrix} \mathbf{0}_6 & \\ & \mathbf{I}_n \end{bmatrix} \quad (45)$$

and  $\boldsymbol{\xi}_b \in \text{SE}(3)$  denotes the pose of the floating base with respect to the inertial reference frame,  $\boldsymbol{\theta} \in \mathbb{R}^n$  denotes the joints' angles,  $\mathbf{v}_b$  is the twist of the base,  $H(\mathbf{q})$  is the generalized mass matrix,  $C(\mathbf{q}, \nu)$  and  $g(\mathbf{q})$  are the Coriolis, centrifugal, and gravitational terms,  $S$  is the selection matrix indicating the actuated degrees of freedom,  $\boldsymbol{\gamma}_c \in \mathbb{R}^k$  is the external contact constraint force vector, and  $J_c(\mathbf{q}) = [J_{cb} \ J_{cs}]$  is the contact Jacobian with  $J_{cb} \in \mathbb{R}^{k \times 6}$  and  $J_{cs} \in \mathbb{R}^{k \times n}$ .

Assuming that we want the floating base or the end effector to behave like a linear mass-spring-damper system when responding to some external forces, we use Cartesian impedance control, e.g., [19], [21], and [22]. In the impedance control law, we add the RL action,

$$F = \Lambda_c \ddot{\mathbf{x}}_d + \Lambda_c \Lambda_d^{-1} [K_d \dot{\mathbf{e}} + K_p \mathbf{e}] + \mathbf{h}_c + \Lambda_c \Lambda_d^{-1} K_{rl} \mathbf{u}_{rl} \quad (46)$$

where  $\Lambda_c$  is the inertia matrix in the operational space,  $\Lambda_d$ ,  $K_d$  and  $K_p$  are the diagonal controller gains that defines the preferred impedance behavior,  $\mathbf{h}_c$  denotes the extra terms in the control law, and  $\mathbf{u}_{rl}$  denotes the RL action.

The torques  $\boldsymbol{\tau}$  are then computed from  $F$  based on the dynamics Eq. (43) or Eq. (44) correspondingly. One can refer to [19], [21], and [22] for more techniques. Here we provide the equations based on which our implementation is designed.

2) *Locomotion*: In the original HIRO paper [3], the high-level policy gives the desired position of the center of mass and desired joint angles every  $c$  steps. The low-level policy produces the torque commands to track the high-level action. Here we adapted HIRO as follows: (1) the high-level policy includes two independent sub-policies: one provides the desired position ( $\mathbf{x}_d$ ) that gives the direction of a desired speed for the low-level policy and the other contact policy provides the contact time. The contact policy is to control the time of two contact modes (stance and swing) within the  $c$  steps, denoted by  $\mathbf{p} \in [-1, 1]$ ; when  $\mathbf{p} > 0$ , the first  $\mathbf{p}c$  steps are in the stance mode and from  $\mathbf{p}c + 1$  to  $c$  in the swing mode; when  $\mathbf{p} < 0$ , the first  $-\mathbf{p}c$  steps are in the swing mode and the rest in stance.

For the low-level control, we employ the control method in [19]. The low-level control includes (1) impedance control with the added RL action in the Cartesian space, (2) projected inverse dynamics which allows us to solve joint motions independently of contact constraints, and (3) quadratic programming to solve physical constraints.

a) *Projected inverse dynamics*: The floating system dynamics Eq. (44) can be transformed into two equations of two orthogonal spaces, *motion space* and *constraint space* via



a projector  $P = I - J_c^\dagger J_c$ . By defining  $\mathbf{h} = C(\mathbf{q}, \boldsymbol{\nu}) + \mathbf{g}(\mathbf{q})$ , the equation for the motion of the system can be written as

$$PM\ddot{\mathbf{q}} + P\mathbf{h} = PB\boldsymbol{\tau} \quad (47)$$

and the other equation for contact constraints

$$(I - P)(M\ddot{\mathbf{q}} + \mathbf{h}) = (I - P)B\boldsymbol{\tau} + J_c^T \boldsymbol{\gamma}_c \quad (48)$$

Note that the torque term in Eq. (48), i.e.,  $(I - P)B\boldsymbol{\tau}$  doesn't contribute to the motion of the system (Eq. (47)). But the torque term in Eq. (47) can affect the constraint equation (Eq. (48)) via  $\ddot{\mathbf{q}}$ . Hence we compute the torques ( $\boldsymbol{\tau}_m = PB\boldsymbol{\tau}$ ) that control the motion behavior via Eq. (47) and then use quadratic programming to compute the  $\boldsymbol{\tau}$  to satisfy the contact constraints.

b) *Cartesian impedance control*: If the Cartesian location of the end effector (denoted by  $\mathbf{x}$ ) is subject to some external disturbance  $F_x$ , we want to prescribe the *motion* at the end effector as

$$\Lambda_d \ddot{\mathbf{e}} + K_d \dot{\mathbf{e}} + K_p \mathbf{e} = F_x \quad (49)$$

where  $\mathbf{e} = \mathbf{x}_d - \mathbf{x}$ .

By defining the constraint inertia matrix  $M_c = PM + I - P$  and denoting the Jacobian of  $\mathbf{x}$  we can rewrite Eq. (47) into

$$M_c \ddot{\mathbf{q}} + P\mathbf{h} - \dot{P}\dot{\mathbf{q}} = PB\boldsymbol{\tau} + PJ_x^T F_x \quad (50)$$

We then pre-multiply Eq. (50) by  $J_x M_c^{-1}$ , replace  $J_x \ddot{\mathbf{q}}$  with  $\ddot{\mathbf{x}} - \dot{J}_x \dot{\mathbf{q}}$ , and multiply by  $\Lambda_c = (J_x M_c^{-1} P J_x^T)^{-1}$ . The resulting equation becomes

$$\Lambda_c \ddot{\mathbf{x}} + \mathbf{h}_c = \Lambda_c J_x M_c^{-1} PB\boldsymbol{\tau} + F_x \quad (51)$$

where  $\mathbf{h}_c = \Lambda_c J_x M_c^{-1} (P\mathbf{h} - \dot{P}\dot{\mathbf{q}}) - \Lambda_c \dot{J}_x \dot{\mathbf{q}}$ . We use  $\tau = J_x^T F$  with  $F$  in Eq. (46), which gives

$$\Lambda_d \ddot{\mathbf{e}} + K_d \dot{\mathbf{e}} + K_p \mathbf{e} + K_{rl} \mathbf{u}_{rl} = 0 \quad (52)$$

By imposing the underactuation constraints  $\boldsymbol{\tau}_m = B\boldsymbol{\tau}$ , we use  $\boldsymbol{\tau}_m = (PB)^\dagger J_x^T F$  with  $F$  in Eq. (46) to control the *motion*. To satisfy contact constraints, we use quadratic programming to minimize  $\|PB\boldsymbol{\tau} - \boldsymbol{\tau}_m\|_2^2$  under constraints.

We use the above controller for both the center of mass and the swing leg. As for the center of the mass, the desired goal  $\mathbf{x}_d$  is given by the high-level policy, which is mapped to the equivalent velocity  $\mathbf{v}_{desired} = v_{speed}(\mathbf{x}_d - \mathbf{x}) / \|\mathbf{x}_d - \mathbf{x}\|$  where  $v_{speed}$  is a given desired speed. As for the swing leg, we followed [20] to compute the desired foot contact location relative to the hip abduction/adduction joints,

$$\mathbf{r}_{desired} = \eta [0.5(\mathbf{v}_{hip} + \mathbf{v}_{com}) - \mathbf{v}_{desired}] \sqrt{\frac{h}{g}} + 0.5 \mathbf{v}_{hip} \delta t \quad (53)$$

where  $h$  is the current height of the hip with respect to the ground,  $\eta$  is a scaling parameter, and  $g$  is the gravitational acceleration. Note that because in our experiments, the velocity of the center of mass is not constant when the gaits are not specified but being learned by a contact policy. So we didn't include the feedback term. Also we used a large desired velocity and a small  $\eta = 0.002$  because of large

noises in the controller. Note that Eq. (53) may not be the optimized contact locations for the ant dynamics but this is a reasonable baseline to start with, given the similarity between the 3-joint 4-legged ant and the quadrupedal robot.

c) *Quadratic programming*: From the *constraint* equation Eq. (48), we can solve for  $\boldsymbol{\gamma}_c$ ,

$$\boldsymbol{\gamma}_c = \boldsymbol{\eta} + \boldsymbol{\rho} \quad (54)$$

where

$$\begin{aligned} \boldsymbol{\eta} &= -(J_c^T)^\dagger (I - P)(I - MM_c^{-1}P)B\boldsymbol{\tau} \\ \boldsymbol{\rho} &= (J_c^T)^\dagger (I - P)[(I - MM_c^{-1}P)\mathbf{h} + MM_c^{-1}\dot{P}\dot{\mathbf{q}}] \end{aligned} \quad (55)$$

The contact constraints include (a) unilateral constraint to avoid loss of contact  $\boldsymbol{\gamma}_{c,z} \geq 0$  and (b) friction cone constraint to avoid slipping  $\mu \boldsymbol{\gamma}_{c,z} \geq \sqrt{\boldsymbol{\gamma}_{c,x}^2 + \boldsymbol{\gamma}_{c,y}^2}$  where  $\mu$  is the friction coefficient at the contact point. Considering the differences in the stance leg and swing leg, the QP becomes

$$\begin{aligned} \min_{\boldsymbol{\tau}} \quad & \frac{1}{2} \|PB\boldsymbol{\tau} - \boldsymbol{\tau}_m\|_2^2 \\ \text{subject to} \quad & \eta_z^i + \rho_z^i \geq 0 \\ & \mu(\eta_z^i + \rho_z^i) \geq \sqrt{(\eta_x^i + \rho_x^i)^2 + (\eta_y^i + \rho_y^i)^2} \\ & \boldsymbol{\tau}_{min} \leq \boldsymbol{\tau} \leq \boldsymbol{\tau}_{max} \end{aligned} \quad (56)$$

where the superscript  $i$  denotes the  $i$ th stance leg and  $\boldsymbol{\tau}_{min}$  and  $\boldsymbol{\tau}_{max}$  are the torque saturations. Note that the above is quadratically constrained quadratic programming. We approximate the friction cone with a linearized 4-edge pyramid, which gives a linearly constrained quadratic programming which can be solved with standard QP solvers.

3) *Manipulation*: In our manipulation experiment, we used force-based control in [21] (without controlling the behavior in the null space). The contact policy and the quadratic programming to satisfy the contact constraints in Fig. 2 are not used. The Cartesian space control is

$$\boldsymbol{\tau} = M\bar{J}[\ddot{\mathbf{x}}_r - \dot{J}\dot{\mathbf{q}}] + C(\mathbf{q}, \dot{\mathbf{q}})\dot{\mathbf{q}} + \mathbf{g} \quad (57)$$

where

$$\begin{aligned} \ddot{\mathbf{x}}_r &= \ddot{\mathbf{x}}_d + K_d(\dot{\mathbf{x}}_d - \dot{\mathbf{x}}) + K_p(\mathbf{x}_d - \mathbf{x}) \\ \bar{J} &= M^{-1}J^T(JM^{-1}J^T)^{-1} \end{aligned} \quad (58)$$

The high level action is defined the same as in locomotion, that is, the absolute position in the Cartesian space, which is used as the direction of a desired speed for low-level control.

### E. Proof and discussion of Theorem 3.

Denoting the  $i^{th}$  components of the diagonal positive definite matrices  $\tilde{\Lambda}_y$  and  $\tilde{B}_y$  by  $\tilde{\lambda}_{y,i}$  and  $\tilde{b}_{y,i}$ , plugging

$$\begin{aligned} \lambda_i &= -\tilde{\lambda}_{y,i} \tilde{b}_{y,i} \\ b_{ii} &= -\tilde{\lambda}_{y,i} K_{rl,i} \end{aligned} \quad (59)$$

into  $(\partial h_i / \partial s_{1i}) b_{ii} + \lambda_i$ , because  $\tilde{b}_{y,i} > 0$ ,  $\tilde{\lambda}_{y,i} > 0$ , and  $(\partial h_i / \partial s_{1i}) K_{rl,i} > \epsilon$ ,

$$\frac{\partial h_i}{\partial s_{1i}} b_{ii} + \lambda_i = -\tilde{\lambda}_{y,i} \left( \frac{\partial h_i}{\partial s_{1i}} K_{rl,i} + \tilde{b}_{y,i} \right) < -\tilde{\lambda}_{y,i} \epsilon \quad (60)$$

TABLE I  
HYPERPARAMETERS IN C-HIRO VS HIRO EXPERIMENTS

Parameter	Ant maze (C-HIRO)	Ant maze (HIRO)	Contact maze(C-HIRO)	Contact maze(HIRO)
$\gamma$ (Discount in value function)	HL: 0.99, LL:0.1	HL: 0.99, LL:0.99	HL: 0.99, LL: 0.99	HL: 0.99, LL:0.99
$\sigma$ (STD in exploration)	HL:1.0, LL:1.0	HL:1.0, LL:1.0	HL:1.0, LL:0.2	HL:1.0, LL:1.0
gradient clipping	0.1	0.1	0.1	0.1
target update period	200	200	100	100
train steps	HL: 400, LL:400	HL: 400, LL:400	HL:100, LL:200	HL:100, LL:200

Hence there exists  $\epsilon_1 = \tilde{\lambda}_{y,i}\epsilon > 0$  that the first inequality in *Theorem 2* is satisfied. When  $(\partial h_i / \partial s_2) K_{rl,i} > \epsilon$ , the second inequality in *Theorem 2* becomes

$$\begin{aligned} & \frac{\partial h_i}{\partial s_{2i}} b_{ii} \\ &= - \frac{\partial h_i}{\partial s_{2i}} \tilde{\lambda}_{y,i} K_{rl,i} \\ &< - \tilde{\lambda}_{y,i} \epsilon \end{aligned} \quad (61)$$

Hence there exists  $\epsilon_1 = \tilde{\lambda}_{y,i}\epsilon > 0$  that *Theorem 2* is satisfied. Because  $W_y$  is identity, the assumption in *Theorem 2* that  $\dot{W}_y$  can be ignored is also satisfied. According to *Theorem 2*, the system is contracting. Proof is finished.

#### F. Environments, Hyperparameters, and Discussions

##### 1) 2D Math Example:

a) *RL hyperparameters*: We use the following hyperparameters:

- entropy coefficient: 0.0
- learning rate: 0.0001,
- vf coefficient: 1.0
- max gradient norm: 0.5
- gamma:0.99
- lambda: 0.95
- No. of minibatches (nminibatches): 4
- clip range:0.1
- No. of optimized epoches (noptepochs): 10

As for the parameters not listed, we used the default parameters from the OpenAI baselines package.

b) *Environments*: The coefficients of the system dynamics Eq. (27) are  $\tau_z = 0.0437$ ,  $\tau_x = 0.01$ ,  $K_1 \in [-0.01, 0.01]$ ,  $K_2 \in [-0.01, 0.01]$ ,  $x \in [1, 3]$ ,  $z \in [-3, 1]$ , and  $K_{sur} \in [1, 31]$ .

We tested different RL state space designs: (a)  $[x \ f]$ , (b)  $[e_x \ e_f]$ , (c)  $[e_x \ e_f \ \sum e_x \ \sum e_f]$  without NN weight constraints, and (d)  $[e_x \ e_f \ \sum e_x \ \sum e_f]$  with NN weight constraints. The first two failed to reach 100% success rate (error < 0.4). The above results are from (c) and (d).

c) *Theorem 4*: To avoid non-zero error equilibriums, Fig. 4 (f), we develop *Theorem 4* as follows: Given the nonlinear dynamics  $\dot{e} = f(e, u, t)$ ,  $s_1 = e$ , and  $s_2 = \int_0^t e dt$ , We approximate the nonlinear dynamics with a time-invariant  $\pi$  by its locally linearized model,

$$\begin{aligned} \dot{e} &= \frac{\partial f}{\partial e} e + \frac{\partial f}{\partial u} u + \frac{\partial f}{\partial t} t \\ \dot{u} &= \frac{\partial \pi}{\partial s_1} \dot{e} + \frac{\partial \pi}{\partial s_2} e \end{aligned} \quad (62)$$

Assuming  $\frac{\partial f}{\partial t} t$  converges to  $f_{stable}$  as  $t$  approaches infinity, the steady states ( $\dot{e} = 0$  and  $\dot{u} = 0$ ) are

$$\begin{cases} e = 0 \\ \frac{\partial f}{\partial u} u + f_{stable} = 0 \end{cases} \quad \text{and} \quad \begin{cases} \frac{\partial \pi}{\partial s_2} = 0 \\ \frac{\partial f}{\partial e} e + \frac{\partial f}{\partial u} u + f_{stable} = 0 \end{cases} \quad (63)$$

Without using  $W_e$ ,  $W_u$ , and  $\pi_z$ , one can limit the static equilibrium of the system to be only at the desired value. Here we state the sufficient condition, *Theorem 4*.

**Theorem 4** If in the entire working space,

- there exists  $u$  in the control policy action space that

$$\frac{\partial f}{\partial u} u + f_{stable} = 0 \quad (64)$$

- for everywhere in the action space,

$$\frac{\partial \pi_z}{\partial s_2} \neq 0 \quad (65)$$

Eq. (1) has one and only one static equilibrium at the desired value, i.e.,  $e = 0$ .

##### 2) Ant maze and contact maze:

a) *RL hyper-parameters*: We use the same set of parameters as in the HIRO paper except those in Table. I:

In the contracting policy, we use a  $3 \times 400$  MLP for each axis. Other networks are the same as the HIRO paper.

b) *Environments*: The ant maze is from  $x \in (-1, 12)$  and  $y \in (-1, 14)$  and the ant is randomly put inside the maze initially. The target is randomly sampled inside  $x \in (1, 8)$  and  $y \in (2, 11)$ , the right-side area with more blocks. The success is defined as the L2 norm of distance is smaller than 2. The ant has 3-joint legs. The first two are at the hip within range of 60 degrees ( $z$  direction) and 10 degrees in the perpendicular plane at the neural hip position. The third joint is the kneel at the leg within range of 40 degrees in the same perpendicular plane at the neural hip position. In the contact maze, the target is sampled between  $x \in (0.41, 0.415)$ ,  $y \in (-0.025, -0.02)$ , and  $z \in (0.005, 0.015)$  (centered at the green box) with the success defined as the L2 norm is less than 0.005. The 7-DOF robot used is the Franka panda robot.

#### ACKNOWLEDGMENTS

This study was supported in part under the RIE2020 Industry Alignment Fund – Industry Collaboration Projects (IAF-ICP) Funding Initiative, as well as cash and in-kind contribution from the industry partner, HP Inc., through the HP-NTU Digital Manufacturing Corporate Lab.

## REFERENCES

- [1] W. Lohmiller and J.-J. E. Slotine, "On contraction analysis for nonlinear systems," *Automatica*, vol. 34, no. 6, pp. 683–696, 1998.
- [2] J. Schulman, F. Wolski, P. Dhariwal, A. Radford, and O. Klimov, "Proximal policy optimization algorithms," *arXiv preprint arXiv:1707.06347*, 2017.
- [3] O. Nachum, S. S. Gu, H. Lee, and S. Levine, "Data-efficient hierarchical reinforcement learning," *Advances in neural information processing systems*, vol. 31, 2018.
- [4] F. Berkenkamp, M. Turchetta, A. P. Schoellig, and A. Krause, "Safe model-based reinforcement learning with stability guarantees," *arXiv preprint arXiv:1705.08551*, 2017.
- [5] M. Jin and J. Lavaei, "Stability-certified reinforcement learning: A control-theoretic perspective," *IEEE Access*, vol. 8, pp. 229 086–229 100, 2020.
- [6] S. A. Khader, H. Yin, P. Falco, and D. Kragic, "Stability-guaranteed reinforcement learning for contact-rich manipulation," *IEEE Robotics and Automation Letters*, vol. 6, no. 1, pp. 1–8, 2020.
- [7] N. M. Boffi and J.-J. E. Slotine, "Implicit Regularization and Momentum Algorithms in Nonlinearly Parameterized Adaptive Control and Prediction," *Neural Computation*, vol. 33, no. 3, pp. 590–673, 03 2021. [Online]. Available: <https://doi.org/10.1162/neco.a.01360>
- [8] S. Singh, S. M. Richards, V. Sindhvani, J.-J. E. Slotine, and M. Pavone, "Learning stabilizable nonlinear dynamics with contraction-based regularization," *The International Journal of Robotics Research*, vol. 40, no. 10-11, pp. 1123–1150, 2021.
- [9] I. R. Manchester, M. Revay, and R. Wang, "Contraction-based methods for stable identification and robust machine learning: a tutorial," *arXiv preprint arXiv:2110.00207*, 2021.
- [10] D. Sun, S. Jha, and C. Fan, "Learning certified control using contraction metric," *arXiv preprint arXiv:2011.12569*, 2020.
- [11] H. Tsukamoto, S.-J. Chung, and J.-J. E. Slotine, "Contraction theory for nonlinear stability analysis and learning-based control: A tutorial overview," *Annual Reviews in Control*, 2021.
- [12] H. Tsukamoto, S.-J. Chung, J.-J. Slotine, and C. Fan, "A theoretical overview of neural contraction metrics for learning-based control with guaranteed stability," *arXiv preprint arXiv:2110.00693*, 2021.
- [13] I. R. Manchester and J.-J. E. Slotine, "Control contraction metrics: Convex and intrinsic criteria for nonlinear feedback design," *IEEE Transactions on Automatic Control*, vol. 62, no. 6, pp. 3046–3053, 2017.
- [14] —, "Robust control contraction metrics: A convex approach to nonlinear state-feedback  $H^\infty$  control," *IEEE Control Systems Letters*, vol. 2, no. 3, pp. 333–338, 2018.
- [15] —, "Control contraction metrics and universal stabilizability," *IFAC Proceedings Volumes*, vol. 47, no. 3, pp. 8223–8228, 2014.
- [16] H. Tsukamoto, S.-J. Chung, and J.-J. E. Slotine, "Neural stochastic contraction metrics for learning-based control and estimation," *IEEE Control Systems Letters*, vol. 5, no. 5, pp. 1825–1830, 2020.
- [17] P. Zhao, A. Lakshmanan, K. Ackerman, A. Gahlawat, M. Pavone, and N. Hovakimyan, "Tube-certified trajectory tracking for nonlinear systems with robust control contraction metrics," *arXiv preprint arXiv:2109.04453*, 2021.
- [18] B. T. Lopez, J.-J. E. Slotine, and J. P. How, "Dynamic tube mpc for nonlinear systems," in *2019 American Control Conference (ACC)*, 2019, pp. 1655–1662.
- [19] G. Xin, W. Wolfslag, H.-C. Lin, C. Tiseo, and M. Mistry, "An optimization-based locomotion controller for quadruped robots leveraging cartesian impedance control," *Frontiers in Robotics and AI*, vol. 7, p. 48, 2020.
- [20] C. Gehring, S. Coros, M. Hutter, M. Bloesch, M. A. Hoepflinger, and R. Siegwart, "Control of dynamic gaits for a quadrupedal robot," in *2013 IEEE international conference on Robotics and automation*. IEEE, 2013, pp. 3287–3292.
- [21] J. Nakanishi, R. Cory, M. Mistry, J. Peters, and S. Schaal, "Operational space control: A theoretical and empirical comparison," *The International Journal of Robotics Research*, vol. 27, no. 6, pp. 737–757, 2008.
- [22] B. Siciliano and L. Villani, *Robot force control*. Springer Science & Business Media, 1999.